IOP Publishing Plasma Physics and Controlled Fusion

Plasma Phys. Control. Fusion **56** (2014) 095020 (9pp) doi:10.1088/0741-3335/56/9/095020

Particle simulation of lower hybrid wave propagation in fusion plasmas

J Bao[1,2], Z Lin[2,4], A Kuley[1,2] and Z X Lu[3,5]

[1] Fusion Simulation Center and State Key Laboratory of Nuclear Physics and Technology, Peking University, Beijing 100871, People's Republic of China
[2] Department of Physics and Astronomy, University of California, Irvine, CA 92697, USA
[3] Center for Momentum Transport and Flow Organization, UCSD, La Jolla, CA 92093, USA

E-mail: zhihongl@uci.edu

Received 6 November 2013, revised 19 March 2014
Accepted for publication 23 June 2014
Published 6 August 2014

Abstract

Global particle simulations of the lower hybrid (LH) waves have been carried out using fully kinetic ions and drift kinetic electrons with a realistic electron-to-ion mass ratio. The LH wave frequency, mode structure, and electron Landau damping from the electrostatic simulations agree very well with the analytic theory. Linear simulation of the propagation of a LH wave-packet in the toroidal geometry shows that the wave propagates faster in the high field side than the low field side, in agreement with a ray tracing calculation. This poloidal asymmetry arises from the non-conservation of the poloidal mode number due to the non-uniform magnetic field. In contrast, the poloidal mode number is conserved in the cylindrical geometry with the uniform magnetic field.

Keywords: plasma waves, RF heating, Landau damping

(Some figures may appear in colour only in the online journal)

1. Introduction

Radio frequency (RF) waves are considered to be one of the most efficient tools for steady state operation of the tokamak, especially for heating and current drive [1–3]. Wide varieties of linear and quasi-linear simulation models, e.g., the Wentzel–Kramers–Brillouin (WKB, i.e., ray tracing) [4–7], mixed WKB-full-wave [8, 9], beam tracing [10, 11] and full-wave methods [12, 13] have been constructed to study the RF wave propagation and absorption in fusion plasmas during last two decades. However, with the availability of high RF power, the nonlinear phenomena of RF waves become important to heating and current drive. For example, parametric decay instabilities of the lower hybrid (LH) waves have been observed in some experiments [14–19]. A series of theoretical works have studied the nonlinear phenomena related to LH waves [20, 21]. With the rapid increase of the computer power, particle simulation models have been developed to investigate the nonlinear issues related to RF heating and current drive in the slab geometry [22, 23].

In this work, we have developed a particle simulation model for the nonlinear RF physics by utilizing the existing physics capability, toroidal geometry and computational power of the gyrokinetic toroidal code (GTC) [24]. GTC has been widely applied to investigate turbulent transport [24–28] and energetic particle physics [29, 30] in fusion plasmas, in which ions are treated as gyro-centers using the gyrokinetic equation (for frequency lower than ion cyclotron frequency) [31]. However, the gyrokinetic ion model is not suitable for studying RF waves of which frequencies are higher than the ion cyclotron frequency. On the other hand, due to the difference in temporal and spatial scales of ions and electrons, fully kinetic description for both species is not efficient for the mode frequency between electron and ion cyclotron frequency. Thus a new simulation model has been developed in GTC to study RF waves in tokamaks, in which ions are treated as fully kinetic particles and electrons are treated as guiding centers by assuming that RF wavelength (i.e., LH wave) is much longer than electron gyro-radius [32]. This model can handle the physics of the LH wave and ion

[4] Author to whom correspondence should be addressed.

[5] Present address: Plasma Physics Laboratory, Princeton University, PO Box 451, Princeton, NJ 08543, USA.

Bernstein wave with a frequency smaller than the electron cyclotron frequency. In order to overcome the numerical problems generated by the realistic electron-to-ion mass ratio, the high frequency Langmuir oscillation and electron cyclotron motion are removed in the current formulation. The current electrostatic model is only valid to study LH wave propagation in tokamak core plasma, where electrostatic approximation of the LH wave can be satisfied. In this paper, the previous work [32] has been extended to verify the dispersion relation of the LH wave with finite parallel wave vector and the linear electron Landau damping. We have carried out the particle simulations of the LH wave propagation in both the cylindrical and toroidal geometries for the first time. As a benchmark exercise, we launch the LH wave from the tokamak edge to illustrate the difference of LH wave propagation between high and low field sides. We find that the poloidal mode number of the LH wave is not conserved due to the poloidal asymmetry in the toroidal geometry. The wave propagates faster in the high field side than the low field side, which is in agreement with well-known results obtained before by WKB simulations [4, 33]. On the other hand, the poloidal mode number of the LH wave is constant in the cylindrical geometry due to its poloidal symmetry. As the first step of developing the RF simulation model in GTC, all simulations performed in this paper are linear.

An outline of the paper follows. A fully kinetic ion and drift kinetic electron simulation model is presented in section 2. Section 3 describes the dispersion relation of the LH wave and its Landau damping on electrons in the cylindrical geometry. Section 4 presents the GTC simulation of the LH wave propagation in both the cylindrical and toroidal geometries, and its comparison with the WKB simulation. We summarize the results in section 5.

2. Physics model for the LH wave simulation

In this paper, ion dynamics is described by the six-dimensional Vlasov equation [32]:

$$\left[\frac{\partial}{\partial t}+\dot{\mathbf{x}}\cdot\nabla+\frac{Z_{\mathrm{i}}}{m_{\mathrm{i}}}\left(\mathbf{E}+\mathbf{v}\times\mathbf{B}\right)\cdot\frac{\partial}{\partial\mathbf{v}}\right]f_{\mathrm{i}}(\mathbf{x},\mathbf{v},t)=0, \tag{1}$$

where f_{i}, Z_{i} and m_{i} are the ion distribution function, ion charge and mass, respectively. We use the particle coordinates $\mathbf{x}(r,\theta,\zeta)$, where r stands for radial position, θ stands for the poloidal angle and ζ stands for the toroidal angle of the toroidal geometry with circular cross section, respectively. $\mathbf{B}=B\mathbf{b}=B_\theta\mathbf{e}_\theta+B_\zeta\mathbf{e}_\zeta$ is the equilibrium magnetic field. Equations of motion for ions are described as follows:

$$\dot{\mathbf{x}}=\mathbf{v}, \tag{2}$$

$$\dot{\mathbf{v}}=\frac{Z_{\mathrm{i}}}{m_{\mathrm{i}}}\left(-\nabla\phi+\mathbf{v}\times\mathbf{B}\right), \tag{3}$$

where ϕ is the electrostatic potential. In the LH frequency range (i.e., $\omega_{\mathrm{ci}}\ll\omega_{\mathrm{LH}}\ll\omega_{\mathrm{ce}}$, where ω_{ci}, ω_{LH} and ω_{ce} stand for the ion cyclotron, LH wave resonant and electron cyclotron frequency, respectively), ions are considered to be fully unmagnetized. So the second term on the right-hand side of equation (3) is dropped in this work.

The drift kinetic description of the electron is valid for the LH wave since $\omega_{\mathrm{LH}}\ll\omega_{\mathrm{ce}}$, $k\rho_{\mathrm{e}}\ll1$, where k and ρ_{e} are the wave vector of LH wave and electron gyro-radius, respectively. So electron dynamics is described by the five-dimensional drift kinetic equation [31]:

$$\left[\frac{\partial}{\partial t}+\dot{\mathbf{X}}\cdot\nabla+\dot{v}_{||}\frac{\partial}{\partial v_{||}}\right]f_{\mathrm{e}}(\mathbf{X},v_{||},\mu,t)=0, \tag{4}$$

where f_{e} is the electron distribution function. The five-dimensional phase space is defined by the position $\mathbf{X}(r,\theta,\zeta)$, the magnetic moment ($\mu$) and the parallel velocity ($v_{||}$) of the guiding center. The evaluation of f_{e} is described by the equations of the electron guiding center motion as follows:

$$\mathbf{X}=v_{||}\mathbf{b}+\mathbf{v}_{\mathrm{E}}+\mathbf{v}_{\mathrm{c}}+\mathbf{v}_{\mathrm{g}}, \tag{5}$$

$$\dot{v}_{||}=-\frac{1}{m_{\mathrm{e}}}\frac{\mathbf{B}^*}{B}\cdot\left(\mu\nabla B-e\nabla\phi\right), \tag{6}$$

where $\mathbf{B}^*=\mathbf{B}+B v_{||}/\omega_{\mathrm{ce}}\nabla\times\mathbf{b}$ and $\mu=m_{\mathrm{e}}v_\perp^2/2B$. The $E\times B$ drift velocity $\mathbf{v}_{\mathrm{E}}$, the curvature drift velocity $\mathbf{v}_{\mathrm{c}}$ and the grad-B drift velocity $\mathbf{v}_{\mathrm{g}}$ are given by [34]

$$\mathbf{v}_{\mathrm{E}}=\frac{c\mathbf{b}\times\nabla\phi}{B}, \tag{7}$$

$$\mathbf{v}_{\mathrm{c}}=\frac{v_{||}^2}{\omega_{\mathrm{ce}}}\nabla\times\mathbf{b}, \tag{8}$$

$$\mathbf{v}_{\mathrm{g}}=\frac{\mu}{(m_{\mathrm{e}}\omega_{\mathrm{ce}})}\mathbf{b}\times\nabla B. \tag{9}$$

The electrostatic potential ϕ is solved by the Poisson equation:

$$\nabla_\perp\cdot\left[\left(1+\frac{\omega_{\mathrm{pe}}^2}{\omega_{\mathrm{ce}}^2}\right)\nabla_\perp\phi\right]=-4\pi(Z_{\mathrm{i}}n_{\mathrm{i}}-en_{\mathrm{e}}). \tag{10}$$

Here, the undesirable high frequency electron plasma oscillation along the magnetic field line has been suppressed by considering $\left|\nabla_\perp^2\right|\gg\left|\nabla_{||}^2\right|$ [35, 36]. The second term on the left-hand side arises from the perpendicular polarization drift of the electron guiding center.

Equations (1)–(10) form a closed system and are used to investigate the linear physics of the LH wave in fusion plasmas.

3. Dispersion relation of the LH wave

3.1. Dispersion relation

Dispersion relation benchmark for the GTC simulation of the LH wave is carried out in the cylindrical geometry (r,θ,z) with the uniform magnetic field in the z direction. The dielectric tensor for magnetized plasmas can be expressed as

$$\overline{\overline{\varepsilon}}=\begin{bmatrix}S & -iD & 0\\ iD & S & 0\\ 0 & 0 & P\end{bmatrix}, \tag{11}$$

where S, P and D are the elements of Stix dielectric tensor [37]. In the cold plasma limit of the LH wave, we have $S=1+\omega_{\mathrm{pe}}^2/\omega_{\mathrm{ce}}^2-\omega_{\mathrm{pi}}^2/\omega^2$, $P=1-\omega_{\mathrm{pe}}^2/\omega^2$ and $D=-\omega_{\mathrm{pe}}^2/(\omega\omega_{\mathrm{ce}})$,

where ω, ω_{pe} and ω_{pi} are the wave, electron plasma and ion plasma frequency, respectively. We take the electrostatic approximation for the LH wave $N^2 \gg |P|$ [37, 38], where $N = ck/\omega$ is the index of refraction. Then the eigenmode equation of the LH wave becomes:

$$\nabla \cdot \left(\overline{\overline{\epsilon}} \cdot \nabla\phi\right) = 0, \tag{12}$$

substituting equation (11) into equation (12), we have [9]

$$\nabla \cdot (S\nabla\phi) + \nabla_{||} \cdot \left[(P - S)\,\nabla_{||}\phi\right] + \nabla \cdot (\mathrm{i}D\mathbf{b} \times \nabla\phi) = 0. \tag{13}$$

The second term on the LHS of equation (13) is mainly due to the parallel response of electrons. The third term vanishes for uniform density and magnetic field. With the boundary condition $\phi(r_0) = \phi(a) = 0$, where r_0 and a are the inner and outer boundaries respectively, equation (13) has the solution:

$$\phi(r, \theta, z) = C\left[J_m(k_\perp r) - \frac{J_m(k_\perp r_0)}{N_m(k_\perp r_0)} N_m(k_\perp r)\right] \mathrm{e}^{\mathrm{i}(m\theta - nz/R)}, \tag{14}$$

where m and n are the poloidal and parallel mode numbers in the cylinder; J_m and N_m are the first and second kind of Bessel functions with the integer order number m; C is the amplitude of the eigenmode. One can write down the eigenvalue as

$$k_\perp = \sqrt{-\frac{n^2}{R^2} - \frac{P - S}{S}\frac{n^2}{R^2}}, \tag{15}$$

here the terms related to m number vanish since the poloidal magnetic field is zero, the eigenvalue $k_\perp = l\pi/(a - r_0)$ (l is integer) can be derived by the boundary condition and the asymptotic solution of equation (14) by referring to Hankel's asymptotic expansions of Bessel function at $k_\perp r \gg 1$, which is the perpendicular wave vector. Substituting S and P into equation (15), we get the LH wave eigen-frequency $\omega = \omega_0$,

$$\omega_0^2 = \omega_{LH}^2\left(1 + \frac{k_{||}^2}{k_\perp^2}\frac{m_i}{m_e}\right), \tag{16}$$

where $k_{||} = n/R$ is the parallel wave vector, $\omega_{LH} = \sqrt{\omega_{pi}^2/\left(1 + \omega_{pe}^2/\omega_{ce}^2\right)}$ is the LH resonant frequency when $k_{||} = 0$. Equation (16) is the cold plasma dispersion relation of the LH wave in the cylindrical geometry.

An artificial antenna in GTC is used as a source to excite LH waves by adding the electric potential $\delta\phi_{ant}(r, \theta, \zeta, t) = \hat{\phi}(r)\cos(m\theta - n\zeta)\cos(\omega_{ant}t)$, where the subscript 'ant' stands for 'antenna'. In the cylindrical geometry, $\zeta = z/R$. According to the driven resonant cavity theory, if the antenna frequency is equal to the eigen-frequency of the system, the excited mode will have the maximal growth of the amplitude [39]. For this benchmark case, plasma density $n_e = n_i = 4.0 \times 10^{13}\,\mathrm{cm}^{-3}$, temperature $T_e = T_i = 40.0\,\mathrm{eV}$ (for cold plasma) and magnetic field $B = 2.5\,\mathrm{T}$ are uniform, $a = 0.3\,\mathrm{m}, R = 1.0\,\mathrm{m}$, $\omega_{pe} = 0.81\omega_{ce}$ and $k_{||}/k_\perp = 0.076$. The $m = 4$, $n = 60$ mode is selected by applying filters in the poloidal and parallel directions. In the simulation, we get the maximal growth of the LH wave amplitude as shown in figure 1(*a*) when the antenna frequency $\omega_{ant} = 0.98\omega_0$, where $\omega_0 = 3.39\omega_{LH}$ is the theoretical LH wave eigen-frequency. The difference is less than 2% between the GTC simulation and the theory. The radial structure of the LH wave from the GTC simulation is consistent with the analytical theory as shown in figure 1(*b*). Figures 1(*c*) and (*d*) are the corresponding poloidal planes of potential structures of the LH wave from theory and from GTC simulation, respectively. All the simulations in this paper are linear and the electron density fluctuation is effectively infinitesimal. It is seen that GTC simulation agrees with the analytical theory very well.

Next, we carry out simulations in different wavelengths and $\omega_{pe}^2/\omega_{ce}^2$ regimes to measure the eigen-frequency of the LH wave. Figure 2(*a*) (fixed $k_\perp a = 238.1$ and $\omega_{pe}^2/\omega_{ce}^2 = 0.66$), figure 2(*b*) (fixed $k_{||}a = 18.0$ and $\omega_{pe}^2/\omega_{ce}^2 = 0.66$) and figure 2(*c*) (fixed $k_{||}a = 18.0$ and $k_\perp a = 238.1$) show the dependency of the LH wave frequency on $k_{||}$, $k_\perp$ and $\omega_{pe}^2/\omega_{ce}^2$, respectively. The benchmark of the dispersion relation is based on cold plasma approximation. In these simulations, $k_{||}v_e/\omega$ varies from 5.6×10^{-3} to 7.5×10^{-3} and $k_\perp v_i/\omega$ varies from 5.9×10^{-4} to 2.8×10^{-3}, thus the kinetic effects from both species can be ignored. Simulation results are not sensitive to the number of particles per cell as shown in figure 2(*d*) ($k_{||}a = 18.0$, $k_\perp a = 238.1$ and $\omega_{pe}^2/\omega_{ce}^2 = 0.66$). Simulation results agree very well with the analytical dispersion relation.

3.2. Linear electron Landau damping

LH waves with a high parallel wave vector ($k_{||}$) can resonate with electrons when the condition $\omega = k_{||}v_e$ is satisfied and thus can deliver their energy to the resonant electrons by the Landau damping. Therefore, the resonant electrons can be accelerated in the parallel direction and can drive the plasma current. To calculate the Landau damping, we need to consider the finite temperature correction to the dielectric tensor. The general dispersion relation of the LH wave is

$$D(\omega + \mathrm{i}\gamma, k) = 0. \tag{17}$$

The linear electron Landau damping rate (γ) can be calculated when $\gamma \ll \omega$ as follows [40]

$$\gamma = -D_I/\frac{\partial D_R}{\partial\omega}, \tag{18}$$

where the real part D_R and the imaginary part D_I are

$$D_R = \left[1 - \frac{\omega_{pe}^2}{\omega^2}\left(1 + \frac{3k_{||}^2v_e^2}{2\omega^2} + \frac{15k_{||}^4v_e^4}{4\omega^4}\right)\right] \times k_{||}^2 + \left[1 + \frac{\omega_{pe}^2}{\omega_{ce}^2} - \frac{\omega_{pi}^2}{\omega^2}\left(1 + \frac{3k_\perp^2v_i^2}{2\omega^2} + \frac{15k_\perp^4v_i^4}{4\omega^4}\right)\right]k_\perp^2, \tag{19}$$

$$D_I = 2\sqrt{\pi}\frac{\omega_{pe}^2\omega}{|k_{||}|\,v_e^3}\mathrm{e}^{-\frac{\omega^2}{k_{||}^2v_e^2}}, \tag{20}$$

where $v_e = \sqrt{2T_e/m_e}$ and $v_i = \sqrt{2T_i/m_i}$ are the thermal velocities of electrons and ions, respectively, and $k_\perp v_i/\omega < 1$ and $k_{||}v_e/\omega < 1$ are assumed. Here, the finite electron and ion temperatures are kept in the real part of the dispersion relation,

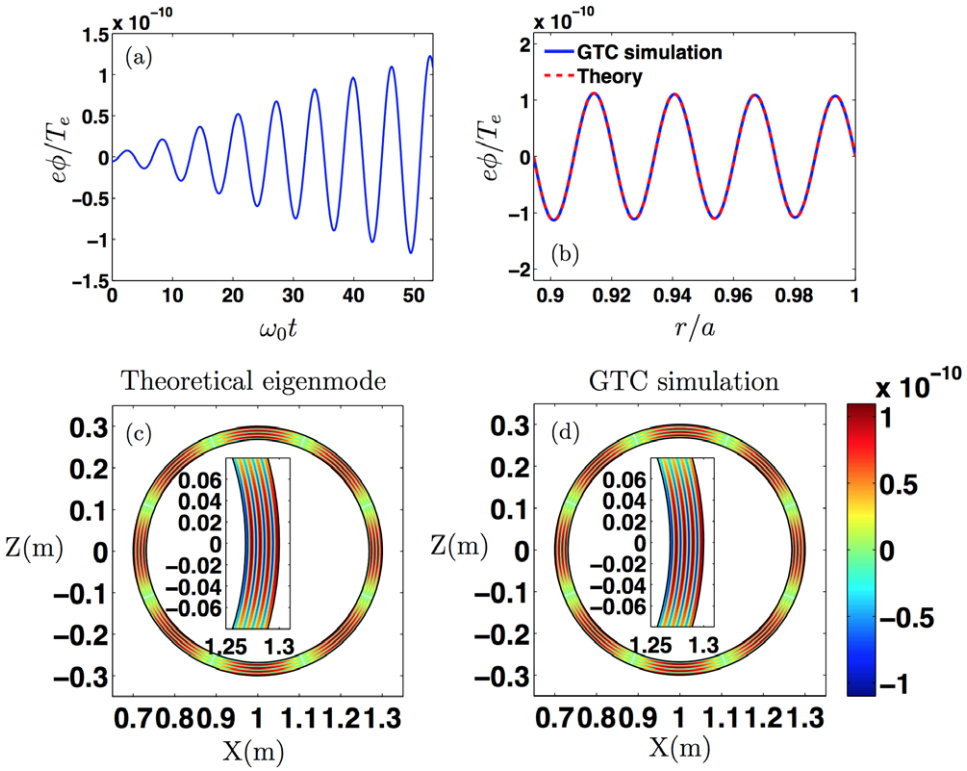

Figure 1. (a) Time evolution of the LH wave ($m = 4, n = 60$) amplitude excited by an artificial antenna in the cylinder, (b) radial profiles of LH waves from the GTC simulation and from the theory. (c) and (d) are poloidal mode structures of LH waves obtained from the theory and from the GTC simulation, respectively. The color scale represents the normalized electrostatic potential $\hat{\phi} = e\phi/T_e$.

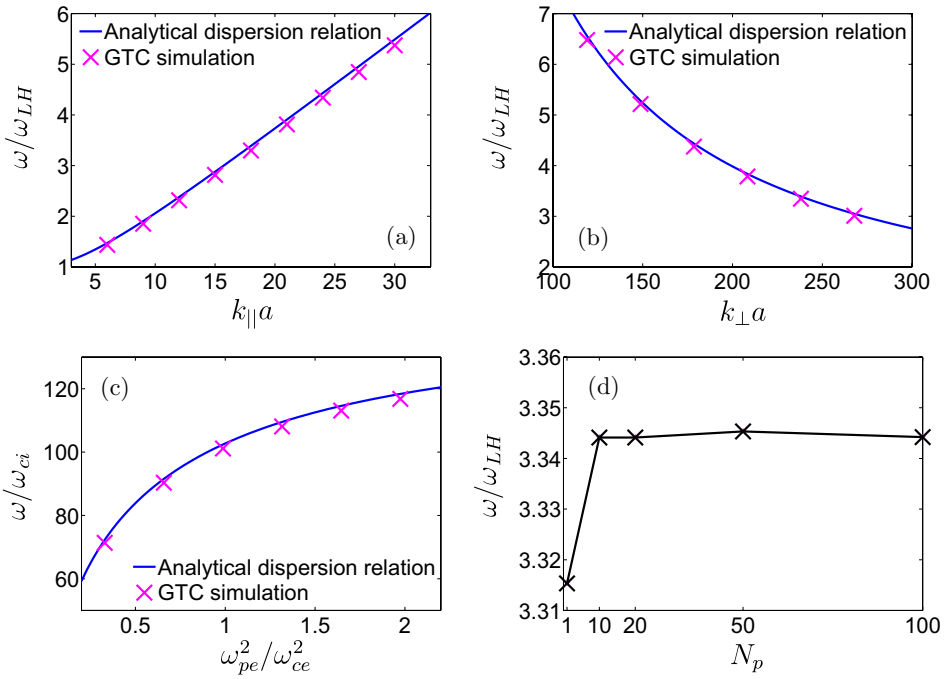

Figure 2. LH wave frequencies as a function of $k_{||}$ (a), $k_{\perp}$ (b) and $\omega_{pe}^2/\omega_{ce}^2$ (c). The red crosses and the blue solid lines are the results from GTC simulation and analytical dispersion relation, respectively, (d) is the convergence of the number of particles per cell N_p for LH wave frequency.

which can affect the LH wave real frequency [41]. We do not include the finite Larmor radius (FLR) correction for the electrons in equation (19) since $k_{\perp}\rho_e \ll 1$ [32, 42, 43].

For verifying the GTC simulation of the electron Landau damping, we focus on the verification of the linear electron Landau damping of a single mode in the cylindrical geometry. We choose the mode number randomly, this has no physical meaning with regard to the real experiments. Other values of mode numbers can also give the results in agreement with theory when $k_{||} \ll k_{\perp}$ is satisfied. The simulation of the

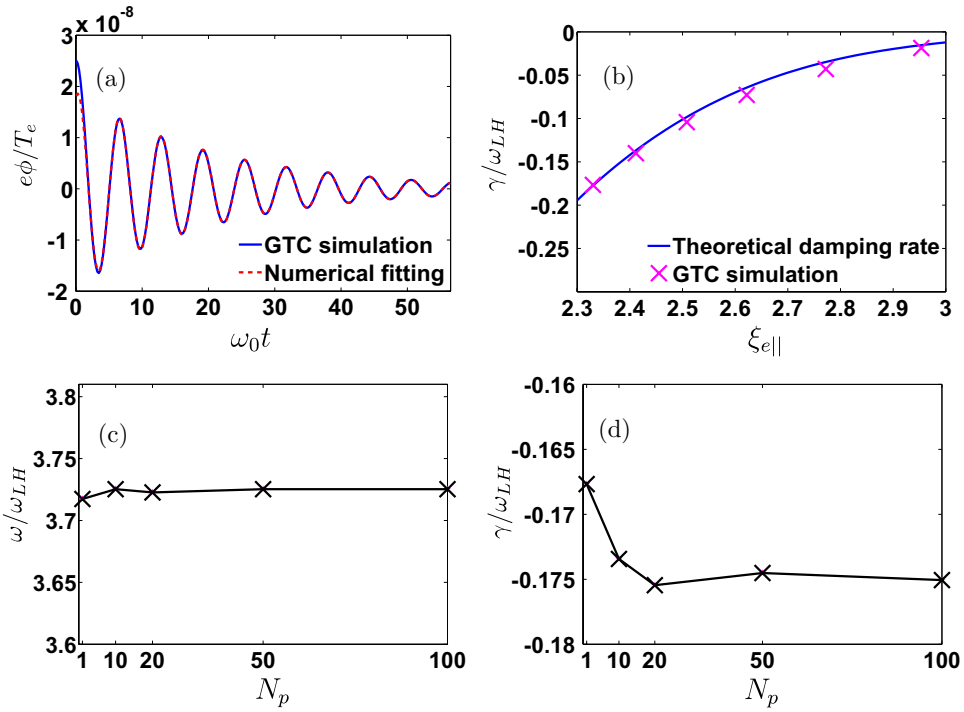

Figure 3. (*a*) Time history of the LH wave amplitude in the simulation. The dashed line is the numerical fitting. (*b*) Comparison of damping rates of LH waves obtained from the GTC simulation and the theoretical calculation in different $\xi_{e||}$ regimes. (*c*) and (*d*) are the convergences of the number of particles per cell N_p for LH wave frequency and damping rate, respectively.

($m = 4$, $n = 100$) LH wave with $k_{||}a = 30.0$, $k_{\perp}a = 448.8$, $\omega_{pe} = 0.51\omega_{ce}$, $\omega_0 = 3.72\omega_{LH}$, $\xi_{i\perp} = \omega_0/k_{\perp}v_i = 6.67$ and $\xi_{e||} = \omega_0/k_{||}v_e = 2.33$ is performed in the cylinder ($a = 0.3$ m and $R = 1.0$ m). Plasma density $n_e = n_i = 1.0 \times 10^{13}\,\mathrm{cm}^{-3}$, temperature $T_e = T_i = 10.0$ keV and magnetic field $B = 2.0$ T are uniform. Here, we choose $n = 100$ in the simulation so that the corresponding $\xi_{e||}$ is small enough for linear Landau damping. The time evolution of the electrostatic potential ϕ of the LH wave in the simulation and a numerical fitting are shown in figure 3(*a*). The fitting function is defined as $\phi(t) = A\cos(\omega t + \alpha)\,e^{\gamma t}$, where ω, γ and α are the real frequency, damping rate, and initial phase of the LH wave, respectively. The damping rates obtained from the theory $\gamma_{ana} = -0.18\omega_{LH}$ and the simulation $\gamma_{simu} = -0.18\omega_{LH}$ are the same. Then we carry out the simulations with $\omega_{pe} = 0.51\omega_{ce}$ in different $\xi_{e||}$ regimes, and compare simulation results of the damping rates with the theoretical calculation as shown in figure 3(*b*). Convergence tests indicate that 20 particles per cell are enough to simulate the linear electron Landau damping as shown in figures 3(*c*) and (*d*). It is well known that the number of particles per wave length in the particle code needs to resolve the Maxwellian distribution function. In our simulation, there are $N_p \times N_r \times N_\theta \times N_z = 20 \times 40 \times 50 \times 50 = 2 \times 10^6$ particles per wavelength, whereN_p, N_r, N_θ and N_z are particle number per cell, grid numbers in radial, poloidal and parallel directions, respectively. 2×10^6 particles per wavelength are enough to resolve the Maxwellian distribution very accurately, which can study the electron Landau damping effectively. Simulation results agree well with the theoretical calculation.

4. LH wave propagation

4.1. Cylindrical geometry

In order to investigate the LH wave propagation in cylindrical plasmas, we apply an antenna as a source term to generate wave-packets at the outer boundary [8, 33] with all the information including the amplitude and initial phase.

We first derive the theoretical wave pattern in the cylinder so that we can compare it with the GTC simulation. An antenna with a Gaussian profile in the poloidal direction is applied in GTC simulation as

$$\phi(r,\theta) = \psi(r)e^{\frac{-(\theta-\theta_0)^2}{\Delta\theta^2}} = \sum_m \Phi_m(r)e^{im\theta}, \qquad (21)$$

where θ_0, $\Delta\theta$ and $\psi(r)$ are the poloidal position, the poloidal width and the amplitude of the antenna, respectively, and $\theta \in [\theta_0 - \pi, \theta_0 + \pi]$. Fourier components of wave-packets generated by the antenna in the poloidal direction can be described as follows

$$\Phi_m(r) = \frac{\Delta\theta}{2\sqrt{\pi}}\psi(r)e^{-im\theta_0 - \frac{m^2\Delta\theta^2}{4}}. \qquad (22)$$

The theoretical wave pattern is considered as the sum of eigenfunctions of equation (13) as

$$\phi(r,\theta) = \sum_m A_m\Psi_m(r)e^{im\theta}, \qquad (23)$$

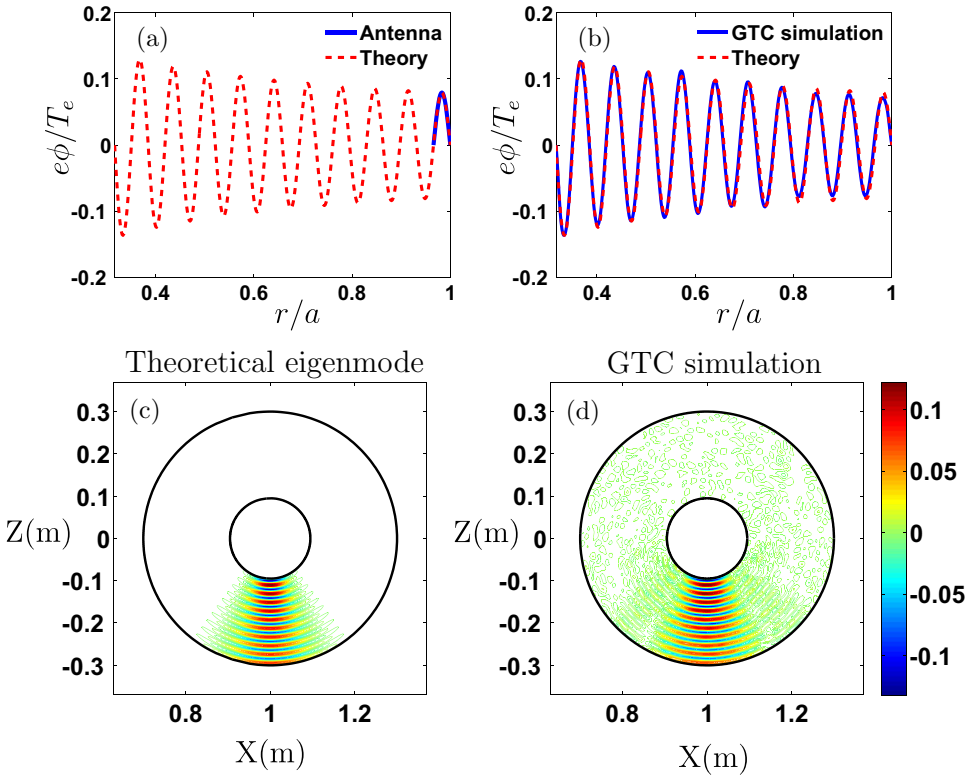

Figure 4. The red dashed line in (*a*) is the theoretical wave pattern and the blue solid line in (*a*) is the radial profile of the artifical perturbation of the antenna. (*b*) is the comparison between radial profiles of wave patterns obtained from GTC simulation and the theory in the cylinder at time $\omega_0 t = 399$. (*c*) and (*d*) are electrostatic mode structures of LH wave patterns in the poloidal plane obtained from the theory and from the GTC simulation, respectively, at time $\omega_0 t = 399$. The color scale represents the normalized electrostatic potential $\hat{\phi} = e\phi/T_e$.

where A_m is the coefficient of every component, and $\Psi_m(r)$ (with a specific m number) is given as (see equation (14))

$$\Psi_m(r) = J_m(k_\perp^{(m)} r) - \frac{J_m(k_\perp^{(m)} r_0)}{N_m(k_\perp^{(m)} r_0)} N_m(k_\perp^{(m)} r). \tag{24}$$

We apply this artificial perturbation (i.e., using antenna) to produce LH wave patterns in the simulation. The LH wave could propagate toward the inner boundary from the antenna and form the theoretical wave pattern. The radial location of the antenna $0.966a \leqslant r \leqslant a$ means that we put our artificial perturbation in the outer region of the radial simulation domain as shown in figure 4(*a*). Combining equations (21)–(24) together, one can write down the coefficient of equation (23) as [9]

$$A_m = \Phi_m(r)/\Psi_m(r), \tag{25}$$

which can be determined at the antenna region.

For a verification case of the LH wave propagation, we apply the parameters: uniform plasma density $n_e = n_i = 4.0 \times 10^{13}\,\mathrm{cm}^{-3}$, temperature $T_e = T_i = 10.0\,\mathrm{eV}$(for cold plasmas) and magnetic field $B = 6.0\,\mathrm{T}$. The simulation is carried out in the cylindrical geometry ($a = 0.3\,\mathrm{m}$ and $R = 1.0\,\mathrm{m}$) with $\omega_{pe} = 0.34\omega_{ce}$, $k_{||}/k_\perp = 0.033$ and $\omega_{ant} = \omega_0 = 1.72\omega_{LH}$. Parallel mode numbers $n = \pm 10$ are applied. There is no energy loss of the LH wave during its propagation, since the plasma is cold. The wave-packets bounce back and forth between the inner and outer boundaries of the simulation domain to produce fluctuation patterns. Finally, the mode structure of the wave pattern is reconstructed in the simulation region. The radial profile of the wave pattern which is obtained from the GTC simulation agrees with the theoretical calculation (see equations (22)–(25)) in figure 4(*b*). The GTC simulation of the LH wave field is shown in figure 4(*d*), which agrees with the theoretical calculation shown in figure 4(*c*). Radial domain contains 10 wavelengths in the current simulation, which is smaller than real experiments.

4.2. Toroidal geometry

Finally, we carry out simulation of the LH wave propagation in the toroidal geometry. The plasma density $n_e = n_i = 8.0 \times 10^{13}\,\mathrm{cm}^{-3}$ and temperature $T_e = T_i = 10.0\,\mathrm{eV}$ (for cold plasmas) are uniform. However, $\mathbf{B} = B_\theta \mathbf{e}_\theta + B_\zeta \mathbf{e}_\zeta$ is non-uniform and the axis value of the magnetic field is $B_a = 6.0T$. Other plasma parameters include $a = 0.36\,\mathrm{m}, R = 1.0\,\mathrm{m}$, $\omega_{pe} = 0.48\omega_{ce}$ and $\omega_0 = 2.99\omega_{LH}$. Toroidal mode numbers $n = \pm 15$ are chosen for this case, which are much smaller than experimental parameters. In this case, we have $N_r = 500$, $N_\theta = 400$ and $N_\zeta = 480$ grid points in the radial, poloidal and toroidal directions, respectively, 20 particles per cell for both species, and the time step satisfies with $\omega_0 \Delta t < 0.06$. We use 11520 cores for the parallel simulation that runs for 1.5 h. Figures 5(*a*) and (*b*) show the propagation of LH waves in the poloidal plane at different time. The structure of the wave-packet is formed by the coupling of different

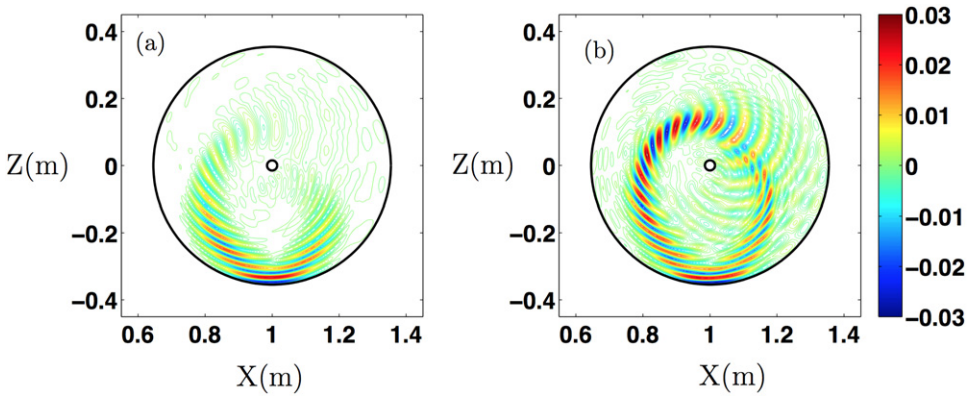

Figure 5. (a), (b) are poloidal contour plots of the normalized electrostatic potential $\hat{\phi} = e\phi/T_e$ from GTC simulation in the toroidal geometry, which show the LH wave propagation at $\omega_0 t = 33$ and $\omega_0 t = 71$ time, respectively.

poloidal harmonics. In the toroidal geometry, the poloidal harmonic number m of the wave-packet is not constant due to the poloidal asymmetry of B [33]. Thus the poloidal position of the wave-packet will change during its propagation as shown in figures 5(a) and (b) even though we launch the wave-packet perpendicular to the poloidal direction [4, 33].

In our simulation, the launched LH wave-packet, which is initially a standing wave pattern in both the parallel and poloidal directions, has both the positive and negative parallel wave vectors ($k_{||}$). Thus the LH wave will propagate along the clockwise and counter-clockwise directions in the poloidal plane because of the two counter-propagations in the parallel direction and their different evolutions of m number. When the LH wave propagates along the poloidal angle, the wave propagates faster in the high field side than the low field side as shown in figures 5(a) and (b). Finally the original standing wave pattern becomes two counter-propagating waves because of the different group velocities in the clockwise and the counter-clockwise directions as the waves propagate toward the magnetic axis. We launch the LH wave from the bottom of the tokamak for benchmarking the code in this case, which is not true for the real experiments.

A WKB simulation [8, 9] gives similar results to the LH wave propagation in the toroidal geometry as shown in figure 6(a). In the WKB simulation, two identical rays are launched along the clockwise and counter-clockwise directions at the same time, respectively. The m number decreases when the ray propagates from low to high field side as shown by the blue solid line in figure 6(b). The black dashed line in figure 6(b) shows that the m number increases when the ray propagates from high to low field side. Figures 6(c) and 6(d) show that the ray propagating in the high field side has a larger radial and poloidal group velocity than the low field side, respectively.

In contrast, the poloidal position of the wave-packet does not change in the cylinder during its propagation (see figure 4(d)), since the poloidal mode number m does not change due to the poloidal symmetry of the equilibrium magnetic field. Therefore, the standing wave pattern in the poloidal direction is maintained during its propagation in the cylinder.

5. Summary

The linear global particle simulation of LH waves has been successfully carried out by using fully kinetic ion and drift kinetic electron simulation model in GTC. Antenna excitation provides the verification of the mode structure of the LH wave, and the linear dispersion relation of the LH wave is well verified by the initial perturbation method. The linear electron Landau damping of the LH wave is verified in the presence of the finite temperature effect in our simulation, and it agrees well with the theory. GTC simulations of the LH wave propagation are performed in both the cylindrical and toroidal geometries. The comparison of the wave pattern shows a good agreement between the simulation and the theory. The structure of the wave pattern is formed due to the coupling of different m harmonics. In the toroidal geometry, the m number is not constant due to the poloidal asymmetry of the equilibrium magnetic field, and its evolution depends on the strength of the magnetic field and the magnetic shear. The wave propagates faster in the high field side than the low field side, which agrees with the WKB simulation. On the other hand, in the cylindrical geometry, the mode number m does not change due to the poloidal symmetry of the equilibrium magnetic field.

Particle simulation approach provides a useful tool to study nonlinear wave-particle interaction, momentum and energy transport induced by RF waves in tokamak. However, computational demand of this approach is huge for simulating real experiments. The numbers of the grid points in radial, poloidal and toroidal direction (i.e., N_r, N_θ and N_ζ) are of the order of 1000 each for real experiments. These simulations require petascale computers on which GTC can run efficiently. The electrostatic approximation is not valid in the edge region, and electrostatic description of the LH wave also excludes some key physics such as mode conversion. Thus, we will next focus on the electromagnetic simulation and the nonlinear effects related to the LH wave.

Acknowledgments

JB acknowledges useful discussions with L Chen, H S Zhang, I Holod, Z X Wang, Y Xiao and W L Zhang. This work was supported by China National Magnetic Confinement Fusion

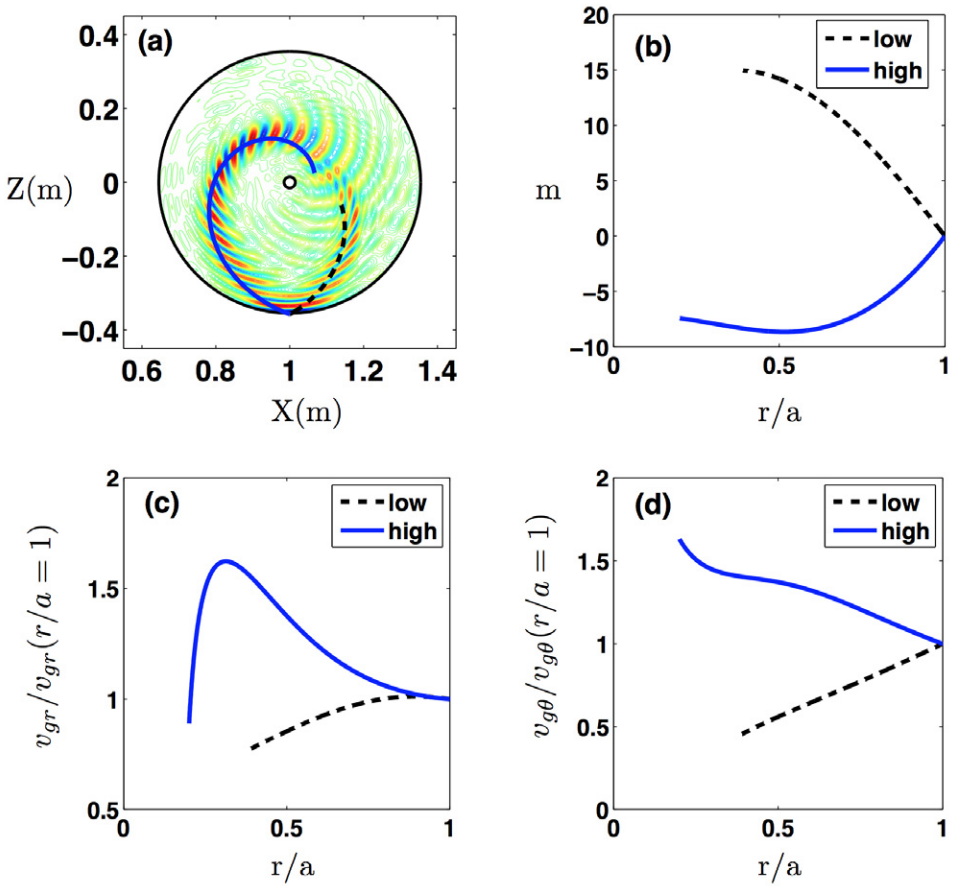

Figure 6. (*a*) WKB simulation of the ray trajectories is compared to GTC simulation in the toroidal geometry. (*b*)–(*d*) are the evolutions of the *m* number, radial group velocity and the poloidal group velocity of the ray, respectively. The blue solid line represents the ray in the high field side, and the black dashed line represents the ray in the low field side.

Science Program (Grant No. 2013GB111000), China Scholarship Council (Grant No. 201306010032), Tri Alpha Energy, Inc. and US Department of Energy (DOE) SciDAC GSEP Center. This research used resources of the Oak Ridge Leadership Computing Facility at Oak Ridge National Laboratory (DOE Contract No. DE-AC05-00OR22725), the National Energy Research Scientific Computing Center (DOE Contract No. DE-AC02-05CH11231), and the National Supercomputing Center in Tianjin.

References

[1] Gormezano C *et al* 2007 *Nucl. Fusion* **47** S285–336
[2] ITER Physics Basis 1999 *Nucl. Fusion* **39** 2495–539
[3] Fisch N J 1987 *Rev. Mod. Phys.* **59** 175–234
[4] Bonoli P T 1984 *IEEE Trans. Plasma Sci.* **12** 95
[5] Bernstein I B 1975 *Phys. Fluids* **18** 320
[6] Ignat D W, Valeo E J and Jardin S C 1994 *Nucl. Fusion* **34** 837
[7] Peysson Y, Decker J and Morini L 2012 *Plasma Phys. Control. Fusion* **54** 045003
[8] Lu Z X, Zonca F and Cardinali A 2012 *Phys. Plasma* **9** 042104
[9] Lu Z X, Zonca F and Cardinali A 2013 *Phys. Plasma* **20** 032115
[10] Pereverzev G V 1992 *Nucl. Fusion* **32** 1091
[11] Bertelli N *et al* 2012 *Phys. Plasmas* **19** 082510
[12] Wright J C, Bonoli P T, Schmidt A E, Phillips C K, Valeo E J, Harvey R W and Brambilla M A 2009 *Phys. Plasma* **16** 072502
[13] Shiraiwa S, Meneghini O, Parker R, Bonoli P T, Garrett M, Kaufman M C, Wright J C and Wukitch S 2010 *Phys. Plasma* **17** 056119
[14] Cesario R and Cardinali A 1989 *Nucl. Fusion* **29** 1709
[15] Napoli F, Castaldo C, Cesario R and Schettini G 2012 *J. Phys.: Conf. Ser.* **401** 012016
[16] Cesario R, Cardinali A, Castaldo C, Paoletti F, Fundamenski W, Hacquin S and the JET-EFDA Workprogramme Contributors 2006 *Nucl. Fusion* **46** 462
[17] Porkolab M *et al* 1977*Phys. Fluids* **20** 2058
[18] Baek S G *et al* 2013 *Plasma Phys. Control. Fusion* **55** 052001
[19] Baek S G *et al* 2014 *Phys. Plasmas* **21** 012506
[20] Kuley A, Liu C S and Tripathi V K 2010 *Phys. Plasmas* **17** 072506
[21] Kuley A and Tripathi V K 2010 *Phys. Plasmas* **17** 062507
[22] Qi L, Wang X Y and Lin Y 2013 *Phys. Plasmas* **20** 062107
[23] Jenkins T G, Austin T M, Smithe D N, Loverich J and Hakim A H 2013 *Phys. Plasmas* **20** 012116
[24] Lin Z, Hahm T S, Lee W W, Tang W M and White R B 1998 *Science* **281** 1835
[25] Xiao Y and Lin Z 2009 *Phys. Rev. Lett.* **103** 085004
[26] Lin Z, Holod I, Chen L, Diamond P H, Hahm T S and Ethier S 2007 *Phys. Rev. Lett.* **99** 265003
[27] Zhang W L, Lin Z and Chen L 2008 *Phys. Rev. Lett.* **101** 095001
[28] Zhang W L, Lin Z and Chen L 2011 *Phys. Rev. Lett.* **107** 239501
[29] Wang Z X, Lin Z, Holod I, Heidbrink W W, Tobias B, Zeeland M V and Austin M E 2013 *Phys. Rev. Lett.* **111** 145003

[30] Zhang H S, Lin Z and Holod I 2012 *Phys. Rev. Lett.* **109** 025001
[31] Brizard A J and Halm T S 2007 *Rev. Mod. Phys.* **79** 421–68
[32] Kuley A, Wang Z X, Lin Z and Wessel F 2013 *Phys. Plasmas* **20** 102515
[33] Bonoli P T and Ott E 1982 *Phys. Fluids* **25** 359
[34] Holod I, Zhang W L, Xiao Y and Lin Z 2009 *Phys. Plasmas* **16** 122307
[35] Lee W W 1987 *J. Comput. Phys.* **72** 243
[36] Lin Y, Wang X Y, Lin Z and Chen L 2005 *Plasma Phys. Control. Fusion* **47** 657
[37] Stix T H 1992 *Waves in Plasmas* (New York: AIP)
[38] Brambilla M 1998 *Kinetic Theory of Plasma Waves: Homogeneous Plasmas* (Oxford: Oxford University Press)
[39] Harris J, Benenson W and Stöcker H 2002 *Handbook of Physics* (New York: Springer)
[40] Chen L 1987 *Waves and Instabilities in Plasmas* (Singapore: World Scienticfic)
[41] Wright J C and Bertelli N 2014 *Plasma Phys. Control. Fusion* **56** 035006
[42] Brambilla M 1976 *Plasma Phys.* **18** 669
[43] Kuehl H H 1976 *Phys. Fluids* **19** 1972